Astronomy & Astrophysics manuscript no. output
February 23, 2026

Unveiling the properties of pulsating low-mass helium-core white dwarfs through TESS asteroseismology I. First results

Leila M. Calcaferro[1,2], Nikoo Hosseininezhad[3], Murat Uzundag[4], Alejandro H. Córsico[1,2], Keaton J. Bell[3,5], Leandro G. Althaus[1,2], and J.J. Hermes[6]

[1] Grupo de Evolución Estelar y Pulsaciones, Facultad de Ciencias Astronómicas y Geofísicas, Universidad Nacional de La Plata, Paseo del Bosque s/n, (1900) La Plata, Argentina
[2] Instituto de Astrofísica La Plata, CONICET-UNLP, Paseo del Bosque s/n, (1900) La Plata, Argentina
[3] City University of New York Graduate Center, 365 5th Ave, New York, NY 10016, USA
[4] Institute of Astronomy, KU Leuven, Celestijnenlaan 200D, 3001, Leuven, Belgium
[5] Physics Department of Queens College, Queens College Science Building, 6530 Kissena Blvd B334, Queens, NY 11367, USA
[6] Department of Astronomy, Boston University, 725 Commonwealth Ave., Boston, MA 02215, USA
e-mail: lcalcaferro@fcaglp.unlp.edu.ar

Received,

ABSTRACT

Context. Recent space-based photometry, particularly from the TESS mission, has transformed the asteroseismological study of pulsating white dwarfs (WDs). In particular, it has opened new possibilities for probing the internal structure of low-mass (LM) helium (He)-core WDs.
Aims. We present a detailed asteroseismological analysis of six pulsating LM WD stars, including new and updated TESS photometry analyzed homogeneously.
Methods. We processed and analyzed TESS observations of TIC 290904838 (J1112), TIC 156064657, TIC 33717565, TIC 344130696, TIC 72637474, and TIC 188087204. We carried out a detailed asteroseismological analysis using fully evolutionary models of LM He-core WDs that allow for varying hydrogen (H)-envelope thicknesses. We also estimated spectroscopic/photometric stellar masses when atmospheric parameters are available.
Results. We report first TESS-based frequencies for J1112 and provide updated/expanded frequency lists for the remaining targets. The asteroseismological analysis yields representative solutions for four stars and provides constrained ranges for the other two. The ensemble spans a broad range of H-envelope thicknesses. For most objects, the derived spectroscopic/photometric stellar masses are compatible with the asteroseismological values.
Conclusions. Our results suggest that pulsating LM WDs display substantial diversity in H-envelope thickness —as in the case of average mass H-rich pulsating WDs— and provide a homogeneous reference framework for future refinements as additional constraints become available.

Key words. asteroseismology — white dwarfs — stars: evolution — stars: interiors

1. Introduction

White dwarf (WD) stars represent the ultimate fate for the vast majority of stars in the Universe, including our Sun (Winget & Kepler 2008; Fontaine & Brassard 2008; Althaus et al. 2010; Saumon et al. 2022). These remnants are the expected outcomes for progenitor stars with masses smaller than $8 - 10.5\ M_{\odot}$, depending on the initial metallicity (e.g., Doherty et al. 2014). Among their many properties, the stellar mass of WDs plays a vital role in astrophysical research, since it constrains the initial-to-final mass relation and is a key ingredient in deriving the WD luminosity function (see e.g., Bedin et al. 2015; García-Berro & Oswalt 2016; Kilic et al. 2017; El-Badry et al. 2018; Cummings et al. 2019). Most WDs have hydrogen (H)-rich atmospheres, and are therefore classified as DA WDs, with an average mass of about $0.6\ M_{\odot}$ and likely carbon-oxygen (CO) cores (Kepler et al. 2016; Tremblay et al. 2016). At the higher end of the mass distribution ($\gtrsim 1\ M_{\odot}$), ultra-massive WDs may instead harbor CO or oxygen-neon (ONe) cores (see e.g., Althaus et al. 2021; Camisassa et al. 2021, 2022; Schwab 2021; Jewett et al. 2025). Conversely, at the low-mass end, helium (He)-core WD stars are characterized by $M_{\star} \lesssim 0.45\ M_{\odot}$ and are often referred to as low-mass (LM) WDs[1] (Althaus et al. 2010).

The formation of LM WDs typically results from binary evolution, occurring through stable mass transfer via Roche-lobe overflow in close binary systems or via unstable mass loss during common-envelope phases (Althaus et al. 2013, 2025; Istrate et al. 2016; Sun & Arras 2018; Li et al. 2019). In both channels, the envelope of the red-giant progenitor is removed before the He flash, so He ignition is avoided and the remnant retains a He core (Althaus et al. 2013; Istrate et al. 2016). Binary evolution is required to explain the lowest-mass systems ($M_{\star} \lesssim 0.3\ M_{\odot}$), since the Universe is not old enough to produce such WDs through single-star evolution. This is particularly true for extremely low-mass (ELM) WDs, often defined as those with $M_{\star} \lesssim 0.18 - 0.20\ M_{\odot}$. While some authors adopt $\sim 0.3\ M_{\odot}$ as

Send offprint requests to: lcalcaferro@fcaglp.unlp.edu.ar

[1] Note that LM WDs with masses higher than $\sim 0.33\ M_{\odot}$ may also harbor CO cores (see e.g., Han et al. 2000; Prada Moroni & Straniero 2009).

the upper mass limit for ELM WDs (see e.g., Brown et al. 2016), here we follow Córsico & Althaus (2014a) (see also Córsico et al. 2019) and define an ELM WD as one whose progenitor did not undergo H-shell flashes. This criterion (which depends on mass and metallicity; see e.g., Serenelli et al. 2002; Istrate et al. 2016), is physically motivated and crucial because the presence or absence of H flashes affects the evolutionary timescales and pulsational properties.

The evolutionary pathways of LM and ELM WDs are pivotal not only for constraining binary interactions but also for their broader impact across various astrophysical contexts. In compact binary systems, LM WDs are expected to play a key role as sources of electromagnetic and gravitational waves, especially for space-based detectors such as the upcoming Laser Interferometer Space Antenna (LISA Amaro-Seoane et al. 2017). Some of these binaries may also represent potential progenitors of Type Ia supernovae (Webbink 1984; Iben & Tutukov 1984; Bildsten et al. 2007).

The number of LM and ELM WDs has steadily increased thanks to large spectroscopic efforts, particularly the ELM Survey, a spectroscopic program designed to identify LM WD binaries using photometry from large sky surveys (Brown et al. 2010, 2012, 2013, 2016, 2020, 2022; Kilic et al. 2011, 2012; Gianninas et al. 2015). Kosakowski et al. (2020) extended the ELM Survey to the southern sky and demonstrated that a Gaia-based approach is effective in detecting ELM WD binaries (see also Kosakowski et al. 2023).

Multi-periodic brightness variations likely produced by global stellar pulsations have been measured in several LM and ELM WDs, defining the class of variable WDs known as ELMVs. To date, more than 20 candidates have been reported (Hermes et al. 2012, 2013b,a; Kilic et al. 2015; Bell et al. 2017, 2018; Pelisoli et al. 2018; Parsons et al. 2020; Lopez et al. 2021; Guidry et al. 2021; Romero et al. 2022; Kosakowski et al. 2023; Bischoff-Kim 2023; Antunes Amaral et al. 2024). The advent of space photometry, and in particular observations from the Transiting Exoplanet Survey Satellite (TESS; Ricker et al. 2015), has expanded the sample of ELMVs and provided new observations of previously known ones (Lopez et al. 2021; Romero et al. 2022, 2025; Bognár & Sódor 2024). Photometric variations have also been detected in stars considered to be probable precursors of LM WDs (pre-ELMVs; e.g., Maxted et al. 2013, 2014; Gianninas et al. 2016; Wang et al. 2020, 2022; Lee et al. 2022). The existence of ELMVs and pre-ELMVs provides us with a unique opportunity to probe the interiors of these stars and test their formation scenarios through asteroseismology (Winget & Kepler 2008; Althaus et al. 2010; Córsico et al. 2019; Bell 2026).

The brightness variations observed in ELMVs are consistent with gravity (g) modes, likely driven by a combination of the $\kappa-\gamma$ (Unno et al. 1989) and convective driving (Brickhill 1991) mechanisms, both occurring in the partial ionization region of H, according to stability analyses (Steinfadt et al. 2010; Córsico et al. 2012; Van Grootel et al. 2013; Córsico & Althaus 2016). Detailed nonadiabatic pulsation computations predict that short-period g modes can also be destabilized by the ϵ mechanism due to stable H burning, particularly for models with $M_\star \lesssim 0.18\ M_\odot$ on their final cooling tracks (Córsico & Althaus 2014b), or before the onset of the CNO flashes, on their early WD cooling branches, in LM WDs with $M_\star > 0.18\ M_\odot$ (Calcaferro et al. 2021).

Asteroseismology of WDs provides stellar parameters by matching observed pulsation periods with theoretical periods from stellar models (e.g., Bell 2026). Fully evolutionary models, evolved self-consistently from the zero-age main sequence (ZAMS), provide a robust framework for this purpose and have been extensively applied by the La Plata Group[2] to several classes of pulsating WDs (see e.g., Córsico et al. 2007a,b, 2008, 2012; Romero et al. 2012; Calcaferro et al. 2017, 2018b, 2024b; Uzundag et al. 2022, 2023). This approach allows the chemical structure and internal stratification to be determined in a fully consistent way. Alternative approaches employ static parametric WD structures (e.g., Giammichele et al. 2018) or parameterized evolutionary models (e.g., Bischoff-Kim et al. 2019). For ELMVs, fully evolutionary models tailored to LM and ELM WDs have been successfully used to probe their internal structure and evolutionary status (Calcaferro et al. 2017, 2018b; Kilic et al. 2018). Other asteroseismological analyses have also been conducted for individual pulsating LM WDs employing the mentioned alternative approaches (see e.g., Su & Li 2023; Bischoff-Kim 2023).

Most evolutionary calculations of LM and ELM WDs are based on progenitor stars that experienced stable mass transfer (Althaus et al. 2013; Istrate et al. 2016), which produce stellar models with thick (canonical) H envelopes that sustain residual stable H burning and thus have extremely long cooling times even at high effective temperatures (Althaus et al. 2013). However, stars with thin H envelopes — unable to sustain residual H burning — are also plausible, as observations suggest (see e.g., Strickler et al. 2009; Irrgang et al. 2021), and would cool to much lower temperatures than their thick-envelope counterparts (e.g. 2500 K vs. 7000 K; Calcaferro et al. 2018a). Motivated by this diversity, Calcaferro et al. (2018b) explored a range of H-envelope masses ($M_{\rm H}$) and showed, through asteroseismology, that some ELMVs are better reproduced with thinner-than-canonical H envelopes. Notably, reducing $M_{\rm H}$ increases $\log g$ for a given $M_\star$, thereby biasing mass estimates derived from $(T_{\rm eff}, \log g)$ if the possible range of envelope thicknesses is not taken into account (Calcaferro et al. 2018a; Althaus et al. 2025). Hence, stellar masses should be inferred using evolutionary tracks that sample the relevant range of $M_{\rm H}$ to avoid systematic offsets.

In this work, we present an updated and homogeneous analysis of TESS photometry and asteroseismology for six ELMV stars: TIC 290904838 (J1112), TIC 156064657, TIC 33717565, TIC 344130696, TIC 72637474, and TIC 188087204. For TIC 290904838 (J1112), we report TESS-based pulsation frequencies for the first time. For the remaining targets, we present new and/or reprocessed TESS short- and ultra-short-cadence observations, and we derive updated frequency solutions for all of them. We then conduct a detailed asteroseismological analysis to constrain the stellar structure and fundamental parameters, in particular, the stellar mass and, importantly, the H-envelope mass, since asteroseismology remains the only method capable of estimating this quantity. To this end, we employ our grid of fully evolutionary models of LM He-core WDs that consider the three relevant parameters at play ($T_{\rm eff}$, $M_\star$, and $M_{\rm H}$; see Calcaferro et al. 2018a,b). Finally, using the asteroseismologically inferred H-envelope mass, we subsequently derive spectroscopic/photometric stellar mass estimates based on the atmospheric parameters available for each star.

This work is organized as follows. In Section 2, we describe the ELMV sample and the data reduction and frequency analysis based on TESS photometry. In Section 3, we carry out a detailed asteroseismological analysis of the sample to constrain the stellar mass and H-envelope mass. In Section 4, we present the

[2] http://evolgroup.fcaglp.unlp.edu.ar/publications.html

spectroscopic/photometric mass estimates. Finally, in Section 5, we summarize and discuss our main results.

2. Target stars and TESS observations

In this Section, we describe the TESS observations and data reduction for the six ELMV targets included in this study. One of these objects is analyzed here for the first time using TESS data, while in most cases, we incorporate additional Sectors not previously considered in the literature. Some of these stars have been analyzed in earlier works (Romero et al. 2022, 2025; Bognár & Sódor 2024); however, we homogeneously reprocess all available data and carry out an independent frequency extraction based on an extended dataset and a refined pre-whitening approach.

Our choice of these six stars was guided by pragmatic considerations: the availability of short- or ultra-short-cadence TESS data covering at least one sector, the presence of more than one independent pulsation mode with S/N above our adopted FAP threshold in preliminary frequency analyses, and the availability of atmospheric parameters. These conditions favor targets with relatively clean but non-trivial pulsation spectra, making them particularly suitable for this first TESS-based asteroseismological study of ELMVs.

Table A summarizes the properties of the six ELMV targets analyzed in this work. For TIC 290904838 (also known as J1112, the second discovered ELMV; Hermes et al. 2013b), we adopt spectroscopic parameters with 3D corrections following Tremblay et al. (2015). The remaining five targets were reported by Romero et al. (2022); for these stars, we adopt Gaia-based atmospheric parameters of $T_{\rm eff}$ and $\log g$ from Gentile Fusillo et al. (2021). The corresponding TESS observations and data reduction are described below.

2.1. Observations and data reduction

In this section, we present the results from our analysis of six LM WDs observed by *TESS*. We used the signal prewhitening code `Pyriod` (Bell 2022) to detect and characterize significant pulsation periods. We adopted the amplitude thresholds recommended by Baran & Koen (2021), corresponding to a 0.1% false-alarm probability (FAP). Any adopted signals falling below this threshold are marked with an asterisk and discussed in the text. For the reported amplitudes and signal-to-noise ratios, we selected the highest value observed across the sectors. For each object, we analyzed all available sectors (prioritizing ultra-short-cadence data where available) and combined per-sector frequency measurements using inverse-variance weighting.

2.1.1. TIC 290904838 (J1112)

This star is the second ELMV discovered and was first identified from high-speed photometric observations at the McDonald Observatory by Hermes et al. (2013b). It exhibited seven pulsation periods spanning from 107 to 2856 s (although the two shortest periods of 107 and 134 s, suggested by Hermes et al. to be possible pressure-mode pulsations, still require confirmation).

We present here the first analysis of TESS data for J1112. This target was observed in three short-cadence (SC) sectors: 45, 46, and 72. No single sector shows a peak above the 0.1% FAP threshold. However, when the light curves are stitched across sectors, the signal-to-noise ratio improves, and two peaks exceed the threshold. The pulsation frequencies derived from our analysis are listed in Table 1. Notably, two of the longest periods reported by Hermes et al. (2013b) are now confirmed by the TESS observations. The amplitude spectrum for this target, based on the stitched light curves of Sectors 45, 46, and 72, is shown in Figure 1 (panel a).

Table 1: Frequencies, periods, amplitudes, and S/N values for TIC 290904838.

ID	Frequency [μHz]	Period [s]	Amplitude [ppt]	S/N
f_0	530.622 ± 0.020	1884.581 ± 0.071	5.231 ± 1.028	5.86
f_1	442.781 ± 0.021	2258.453 ± 0.107	4.965 ± 0.887	5.23

Table 2: Same as Table 1, but for TIC 156064657

ID	Frequency [μHz]	Period [s]	Amplitude [ppt]	S/N
f_0	1227.509 ± 0.029	814.658 ± 0.019	8.108 ± 1.201	5.57
f_1	705.197 ± 0.022	1418.043 ± 0.044	13.414 ± 1.242	9.79
f_2	670.574 ± 0.024	1491.260 ± 0.053	9.495 ± 1.346	6.41
f_3^*	645.957 ± 0.049	1548.110 ± 0.117	6.111 ± 1.241	4.47

Table 3: Same as Table 1, but for TIC 33717565

ID	Frequency [μHz]	Period [s]	Amplitude [ppt]	S/N
f_0	2740.323 ± 0.001	364.920 ± 0.001	19.270 ± 1.845	13.53
f_1	1897.633 ± 0.001	526.972 ± 0.001	11.191 ± 1.176	9.13
f_2	1796.906 ± 0.004	556.512 ± 0.001	9.792 ± 1.171	6.09

2.1.2. TIC 156064657

TESS observed this star in Sector 29 (SC) and Sectors 69 and 96 (both SC and ultra-short cadence, USC). The pulsation frequencies derived from our analysis are listed in Table 2. Figure 1 (panel b) displays the periodogram for Sector 69. We identified a signal in Sector 29 that falls below the significance threshold but is likely a pulsation frequency, labeled as f_3^*. Accepting this signal would increase the FAP to 3.44% (see Appendix B).

For comparison, Romero et al. (2022) analyzed only Sector 29 and reported two periodicities, which we recover (f_1 and f_3^*). By incorporating additional sectors (and USC data), our analysis yields a more complete pulsation set, adding two significant signals (f_0 and f_2).

2.1.3. TIC 33717565

This WD was observed in 35 sectors, comprising both SC and USC data. Given the large number of light curves, we stitched the data by observing year to reduce frequency uncertainties; the comparatively small frequency errors for this target result from this yearly stitching. For the stitched light curves, the 0.1% FAP detection threshold follows the method described by Baran & Koen (2021). The resulting frequencies are listed in Table 3. The periodogram for Year 6 is presented in Figure 1 (panel c).

It is worth noting that Romero et al. (2025) (see also Romero et al. 2022) carried out a frequency analysis for TIC 33717565 using the same sectors and reported a larger set of seven frequencies; however, the corresponding periodogram is not shown. Our analysis confirms two of these signals (f_0 and f_1) and identifies one additional pulsation frequency (f_2).

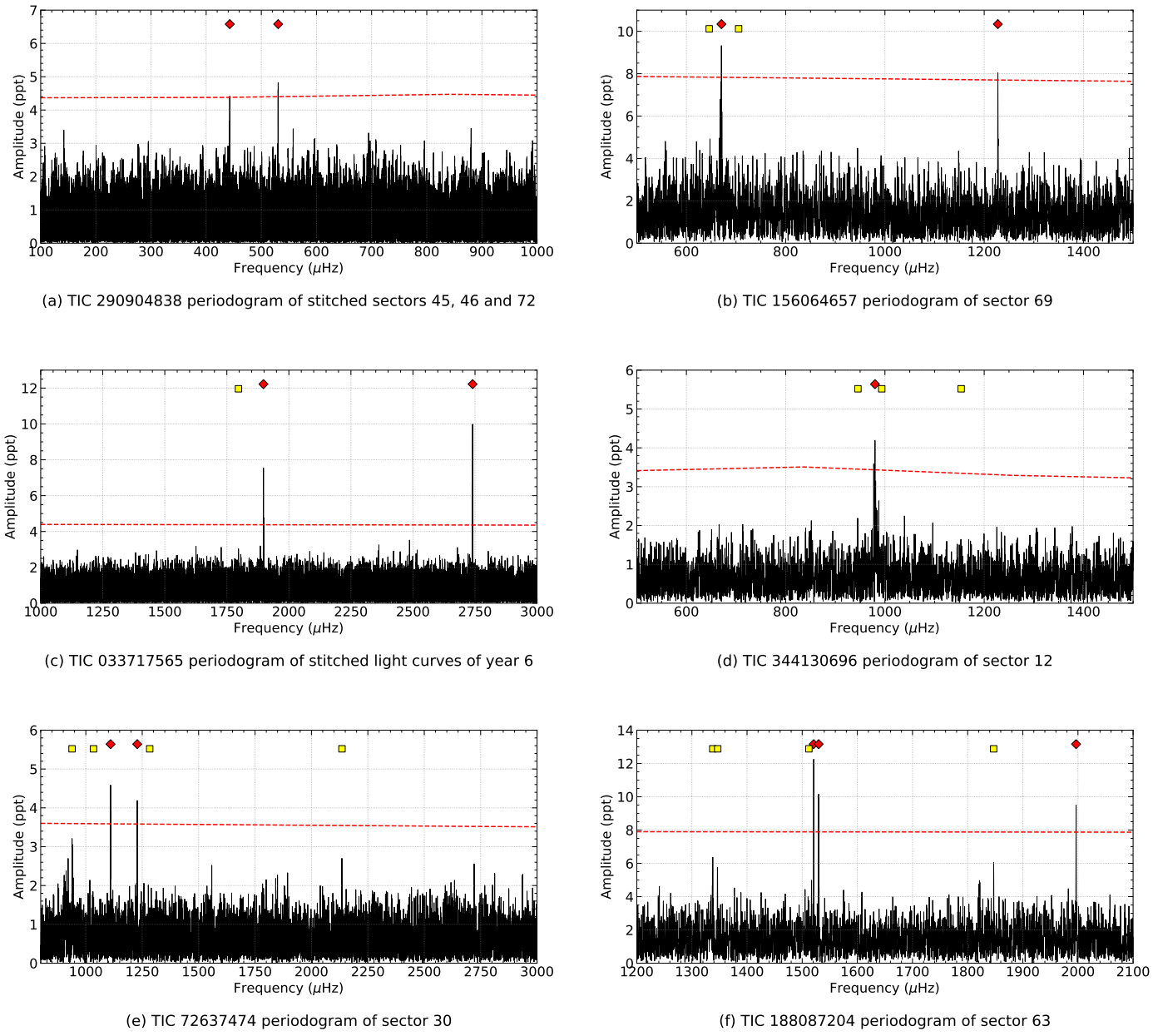

(a) TIC 290904838 periodogram of stitched sectors 45, 46 and 72

(b) TIC 156064657 periodogram of sector 69

(c) TIC 033717565 periodogram of stitched light curves of year 6

(d) TIC 344130696 periodogram of sector 12

(e) TIC 72637474 periodogram of sector 30

(f) TIC 188087204 periodogram of sector 63

Fig. 1: Representative amplitude spectra for each target, selected from the TESS sector (or stitched sectors) that most clearly shows the pulsation signals. Significant frequencies detected in the displayed spectrum are marked with red diamonds. The dashed red line represents the significance threshold. Yellow squares highlight frequencies that were detected in the comprehensive analysis but are weak or not visible in this specific plot.

2.1.4. TIC 344130696

This WD was observed in Sectors 12, 13, 39, 66, 93, and 94. In most sectors, both SC and USC data are available; we prioritized the USC when present. In Sector 93, the data in both cadences are noisy, and no peak above the 0.1% FAP threshold was detected. Two peaks detected in separate sectors appear to trace the same mode (979.972 ± 0.031 and 981.788 ± 0.021 μHz); we averaged them and report the result as f_2. The complete list of frequencies is provided in Table 4. A representative amplitude spectrum from Sector 12 is plotted in Figure 1 (panel d).

Romero et al. (2022) presented a similar analysis, but limited to data from Sectors 12, 13, and 39. We recover their two reported modes (f_2 and f_3). With the expanded dataset, we identify two additional significant signals (f_0 and f_1).

Table 4: Same as Table 1, but for TIC 344130696

ID	Frequency [μHz]	Period [s]	Amplitude [ppt]	S/N
f_0	1153.637 ± 0.033	866.824 ± 0.025	5.829 ± 0.800	5.70
f_1	993.569 ± 0.038	1006.473 ± 0.038	4.101 ± 0.701	5.26
f_2	981.217 ± 0.017	1019.143 ± 0.018	5.112 ± 0.550	7.78
f_3	945.612 ± 0.018	1057.516 ± 0.020	5.692 ± 0.476	10.03

2.1.5. TIC 72637474

TESS observed this object in Sector 3 (SC) and Sectors 30 and 97 (SC and USC). We detected five significant peaks above the 0.1% FAP threshold. We also identified a sixth peak that falls below this threshold but remains astrophysically plausible. In-

Table 5: Same as Table 1, but for TIC 72637474.

ID	Frequency [μHz]	Period [s]	Amplitude [ppt]	S/N
f_0	2135.362 ± 0.017	468.305 ± 0.004	3.14 ± 0.461	5.83
f_1	1283.145 ± 0.011	779.335 ± 0.007	4.94 ± 1.385	9.14
f_2	1228.012 ± 0.031	814.324 ± 0.021	4.154 ± 0.558	6.13
f_3	1109.743 ± 0.028	901.110 ± 0.023	4.535 ± 0.563	6.68
f_4	1034.186 ± 0.042	966.944 ± 0.039	5.022 ± 0.725	6.12
f_5^*	938.952 ± 0.043	1065.017 ± 0.049	3.202 ± 0.001	4.71

Table 6: Same as Table 1, but for TIC 188087204

ID	Frequency [μHz]	Period [s]	Amplitude [ppt]	S/N
f_0	1996.577 ± 0.023	500.857 ± 0.006	9.507 ± 1.274	6.42
f_1^*	1847.156 ± 0.055	541.373 ± 0.016	6.045 ± 1.247	4.43
f_2	1529.837 ± 0.032	653.664 ± 0.014	10.128 ± 1.247	6.78
f_3	1520.877 ± 0.016	657.515 ± 0.007	15.233 ± 1.572	8.11
f_4	1512.081 ± 0.043	661.340 ± 0.019	12.704 ± 1.590	5.21
f_5	1346.797 ± 0.021	742.502 ± 0.012	14.478 ± 3.131	8.25
f_6^*	1337.837 ± 0.051	747.475 ± 0.028	6.377 ± 1.247	4.27

cluding this peak would require relaxing the FAP threshold to 0.857% (see Appendix B). This signal is labeled f_5^* in Table 5. Figure 1 (panel e) shows the periodogram for Sector 30, highlighting the significant frequencies.

For comparison, Romero et al. (2022) analyzed data from Sectors 3 and 30 and reported only three periods, all of which we recover (f_2, f_3, and f_4). With the expanded dataset, we identify two additional significant signals (f_0 and f_1), plus one low-amplitude candidate (f_5^*).

2.1.6. TIC 188087204

This WD was observed in Sectors 63 and 90 (SC and USC) and in Sector 36 (SC). We detected five significant peaks, f_0–f_4, which are listed in Table 6. We also detected two sub-threshold signals in Sectors 63 and 90 that stand out above the surrounding noise in both datasets. The probability of a chance coincidence for a match within $\pm\Delta t$ is $2\Delta t/T$ (where T is the total time baseline), which supports treating them as plausible modes; we therefore label them f_1^* and f_6^*. Including these two peaks raises the single-dataset FAP to 0.902% for f_6^* (the lower-amplitude case in Sector 63; see Appendix B). However, because the same frequency appears in two independent datasets, the combined FAP is significantly smaller. The pulsation spectrum for this star is illustrated in Figure 1 (panel f), using data from Sector 63.

Three primary pulsation frequencies, f_2, f_3, and f_4, exhibit a clear pattern of nearly uniform spacing. Averaging the consecutive separations yields $\Delta f = 8.878 \pm 0.029$ μHz. This structure can be naturally interpreted as a rotationally split triplet, with f_3 as the central ($m = 0$) component. An independent pair, f_5 and f_6^*, shows a consistent spacing of 8.960 ± 0.055 μHz, reinforcing the same pattern, and thus, suggesting the possible presence of an additional, incomplete triplet. On this basis, we treat f_3 as a robust $m = 0$ candidate, while f_5 and f_6^* are considered alternative $m = 0$ identifications for the putative second triplet.

Based on Sector 36 alone, Romero et al. (2022) reported five pulsation modes all of which we recover (f_0, f_1^*, f_3, f_4, and f_5). Both that work and Bognár & Sódor (2024) suggested a possible triplet near 1521 μHz (which we identify as f_2, f_3, and f_4). Our expanded multi-sector analysis not only confirms that structure, but also reveals evidence for an additional incomplete pair of frequencies (f_5 and f_6^*) with consistent spacing.

3. Asteroseismological modeling

The asteroseismological analysis carried out in this work is based on a set of stellar models resulting from the complete evolution of LM He-core WDs computed with the LPCODE stellar evolution code (Althaus et al. 2005, 2009, 2013, 2015). This code computes in detail the complete evolutionary stages leading to the formation of WDs from the ZAMS, allowing for a self-consistent description of the internal structure and chemical stratification. The models of LM WDs we employ in this work include both thick (canonical) and thin H envelopes (see Althaus et al. 2013; Calcaferro et al. 2018b, for details about input physics and evolutionary calculations). Adiabatic pulsation periods for non-radial dipole ($\ell = 1$) and quadrupole ($\ell = 2$) g-modes were computed employing the adiabatic version of the LP-PUL pulsation code (see Córsico & Althaus 2006, for details).

We determine the stellar mass and H-envelope thickness, among other relevant quantities, by identifying the model whose theoretical pulsation periods best reproduce the observed ones (Córsico et al. 2019). The quality of the match between the theoretical periods ($\Pi_k^{\rm T}$) and observed ($\Pi_i^{\rm O}$) is evaluated using a merit function:

$$\chi^2(M_\star, T_{\rm eff}, M_{\rm H}) = \frac{1}{n}\sum_{i=1}^{n} \min\left[(\Pi_i^{\rm O} - \Pi_k^{\rm T})^2\right], \quad (1)$$

being n the number of observed periods. The LM WD model that shows the lowest value of χ^2, if it exists, is adopted as the "best-fit model". For convenience, we also define the root-mean-square period residual,

$$\sigma(M_\star, T_{\rm eff}, M_{\rm H}) \equiv \sqrt{\chi^2}, \quad (2)$$

which measures the average mismatch between observed and theoretical periods in units of seconds; the smaller σ, the better the fit. In this way, we calculate $\chi^2 = \chi^2(M_\star, T_{\rm eff}, M_{\rm H})$ (and thus σ) for stellar masses in the range $0.1554 \lesssim M_\star/M_\odot \lesssim 0.4352$ $M_\odot$. For the effective temperature, we cover the range $13000 \gtrsim T_{\rm eff} \gtrsim 6000$ K, while for the H-envelope thickness, we consider the range $-5.8 \lesssim \log(M_{\rm H}/M_\star) \lesssim -1.7$ (depending on the stellar mass; see Calcaferro et al. 2018b).

Analogously to Calcaferro et al. (2018b), we start our analysis assuming that all the observed periods correspond to g modes associated with $\ell = 1$, and considering the set of observed periods of each target star to compute the quality function given by Eq. (1). Next, we assume that the observed periods correspond to a mixture of $\ell = 1$ and $\ell = 2$ g modes. Since we usually do not find suitable solutions when assuming $\ell = 1$ alone, we display the case in which a combination of $\ell = 1$ and $\ell = 2$ g modes is assumed. In Figures 2 to 8 we show, for each ELMV target, the projection of $\log\sigma$ on the $T_{\rm eff}$–$M_\star$ plane. Each point in these maps corresponds to the value of the H-envelope mass that minimizes σ (equivalently, χ^2) for the given ($T_{\rm eff}$, $M_\star$). The color scale is chosen such that smaller values of $\log\sigma$ denote better fits, and the displayed ranges in $T_{\rm eff}$ have been adjusted to highlight the region of interest around the atmospheric parameters. If a single, well-defined minimum is present for a given star, we adopt the corresponding model as the asteroseismological solution. When multiple possible solutions exist — an expected behavior given that pulsating LM WDs generally show only a few independent modes —, we use an external constraint to select a representative solution and/or to define a range of acceptable models. In this work, we consider the uncertainty in the

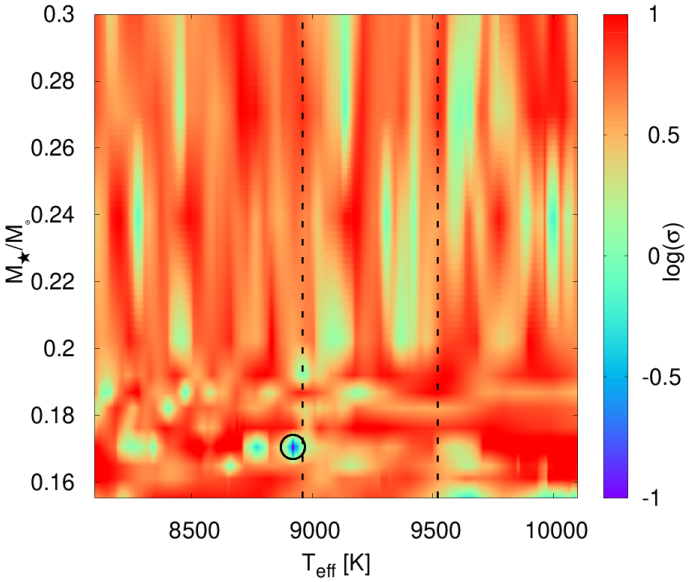

Fig. 2: Projection on the $T_{\rm eff}$ versus $M_\star$ plane of the logarithm of the average period residual (σ) for J1112, assuming that the two periods of J1112 are associated with $\ell = 1, 2$. For each $M_\star$, the value shown corresponds to the H–envelope mass that minimizes the quality function along the explored sequences. Two vertical dashed lines depict the adopted uncertainty for $T_{\rm eff}$. A circle marks the adopted representative solution (when possible).

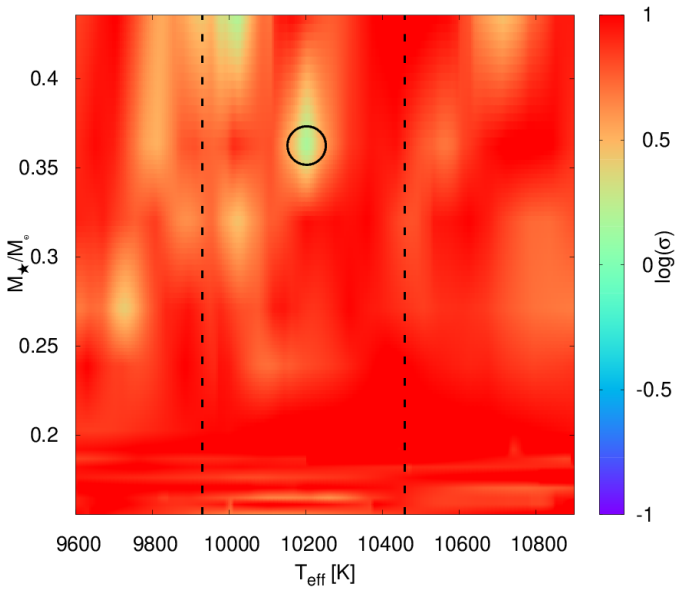

Fig. 3: Same as Fig. 2 but for TIC 156064657 considering the periods from the set S2.

effective temperature, as given by the atmospheric parameters. Specifically, we adopt a $2\sigma_{\rm Teff}$ interval for all targets when selecting representative solutions. Next, we describe the individual results.

3.1. TIC 290904838 (J1112)

Considering the two independent periods observed for this star ($\sim$ 1885 and 2258 s) and reported in Sect. 2.1.1, we have performed period-to-period fits assuming that both correspond to a mix of g modes with $\ell = 1$ and 2, as described above. The results are displayed in Fig. 2. A narrow region of low σ is found along the 0.1706 $M_\odot$ sequence, at effective temperatures slightly lower than the spectroscopic range ($T_{\rm eff}$ = 9240 ± 140 K). The absolute minimum of the quality function (i.e. the smallest σ) occurs at $T_{\rm eff}$ = 8922 K, $M_\star$ = 0.1706 $M_\odot$, and $\log(M_{\rm H}/M_\star) = -5.30$, corresponding to a very thin-H envelope, and yields an average period residual of $\sigma \simeq 0.03$ s. However, consecutive models along the same $(M_\star, M_{\rm H})$ sequence in the range $T_{\rm eff} \sim 8916 - 8928$ K provide comparably good fits, with $\sigma \sim 0.2$ s. Typical changes in the theoretical periods between adjacent grid points are of order 0.1-0.4 s. Residuals much smaller than this, such as $\sigma \sim 0.03$ s, are therefore below the intrinsic resolution of our grid. We therefore regard the consecutive models within this small region as equivalent solutions for our purposes and adopt the solution in the range $T_{\rm eff} \sim 8916 - 8928$ K, with $M_\star = 0.1706\ M_\odot$ and $\log(M_{\rm H}/M_\star) = -5.30$, as representative of J1112. This inference must nevertheless be regarded with caution, as it is based on only two independent observed periods.

3.2. TIC 156064657

Given the set of periods reported in Sect. 2.1.2 for this WD ($\sim$ 815, 1418, 1491, and 1548 s), we considered two subsets of periods for our period-to-period fits. Set S1 comprises the three highest-significance periods, $\sim$ 815, 1418, and 1491 s, which satisfy our original FAP threshold, while set S2 includes all four, adding the $\sim$ 1548 s signal, which becomes acceptable when we relax the FAP criterion.

When using only the three periods in S1 and allowing the full range of $T_{\rm eff}$ of our grid, the global minimum of the quality function occurs at a very low effective temperature ($T_{\rm eff} \sim 9300$ K), well below that of the star ($T_{\rm eff}$ = 10194±132 K), and outside the adopted temperature interval. If we restrict the search to a narrower $T_{\rm eff}$ interval, we find a local minimum near $T_{\rm eff}$ = 10190 K with $M_\star = 0.3624\ M_\odot$ and $\log(M_{\rm H}/M_\star) = -3.10$ (canonical envelope), yielding an average period residual of $\sigma \sim 1.5$ s. However, in this case, additional solutions at lower $T_{\rm eff}$ remain competitive in terms of σ, so the corresponding $\log\sigma$ map does not provide a uniquely preferred solution and is not shown here.

Repeating the procedure with S2 (i.e., including the additional 1548 s period), yields the results shown in Fig. 3. In this case, the global minimum of the quality function — i.e., the best fit over the entire explored parameter space — is found at almost the same $T_{\rm eff}$ as in the S1 case, and roughly at the same $T_{\rm eff}$ of TIC 156064657. This model has $T_{\rm eff}$ = 10202 K, $M_\star = 0.3624\ M_\odot$, and $\log(M_{\rm H}/M_\star) = -3.10$ (canonical envelope) and is characterized by $\sigma \sim 1.4$ s. Although this fit results from the addition of the $\sim$ 1548 s period (obtained after relaxing the FAP criterion), its inclusion improves the overall period match, and the solution is better constrained, as it removes alternative solutions present in the case of S1. We therefore adopt this model as representative of TIC 156064657.

3.3. TIC 33717565

Similarly to the previous cases, we performed period-to-period fits for TIC 33717565 ($T_{\rm eff}$ = 10 676 ± 173 K) using the three periods identified in Sect. 2.1.3 (i.e., $\sim$ 365, 527, and 557 s). We find that the best period fit is located at a very low $T_{\rm eff}$ ($\sim$ 9600 K), in contrast to the adopted temperature interval. Restricting the search to a narrower range of $T_{\rm eff}$, as shown in Fig. 4, reveals multiple possible solutions. Three models are particu-

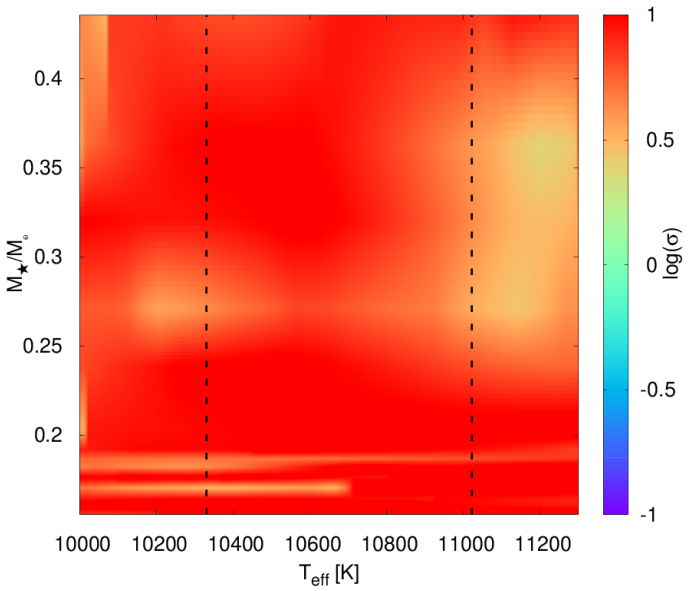

Fig. 4: Same as Fig. 2, but for TIC 33717565.

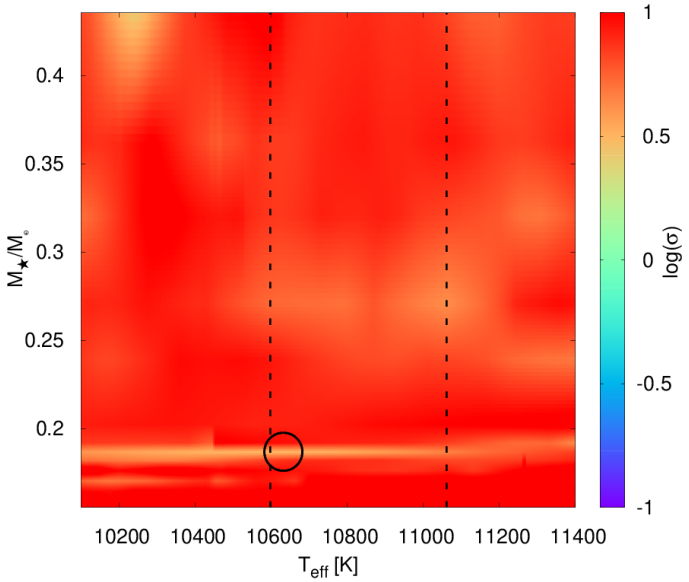

Fig. 5: Same as Fig. 2, but for TIC 344130696.

larly noteworthy. The first has $T_{\rm eff}$ = 11200 K, $M_\star$ = 0.3624 $M_\odot$, $\log(M_{\rm H}/M_\star)$ = −3.10 (canonical envelope), the second, also outside the range of $T_{\rm eff}$, has $T_{\rm eff}$ = 11140 K, $M_\star$ = 0.2707 $M_\odot$, $\log(M_{\rm H}/M_\star)$ = −5.54 (very thin envelope); and the third has $T_{\rm eff}$ = 10658 K, $M_\star$ = 0.1706 $M_\odot$, $\log(M_{\rm H}/M_\star)$ = −2.50 (thin envelope). All three yield comparable average period residuals of a few seconds, with the first two providing slightly better fits but lying outside the adopted $T_{\rm eff}$ range, and the third approximately matching the star's $T_{\rm eff}$. Given this degeneracy, we can only conclude that acceptable solutions span stellar masses in the range 0.1706 − 0.3624 $M_\odot$, $T_{\rm eff}$ in the interval 10660 − 11200 K, and a very poorly constrained H envelope mass between $\sim 3\times10^{-6} M_\star$ and $3\times10^{-3} M_\star$.

3.4. TIC 344130696

We performed period-to-period fits for TIC 344130696 ($T_{\rm eff}$ = 10829 ± 116 K) employing the four periods determined in Sect. 2.1.4 (i.e., ∼ 867, 1006, 1019, and 1058 s). The best period fit, in this case, is located at a very low $T_{\rm eff}$ (∼ 9680 K), well below the adopted range of $T_{\rm eff}$, and is characterized by $\sigma \sim 1.5$. In a narrower range of $T_{\rm eff}$, Fig. 5 reveals the existence of multiple possible solutions. Two models are of particular interest. The first has $T_{\rm eff}$ = 10246 K, $M_\star$ = 0.4352 $M_\odot$, $\log(M_{\rm H}/M_\star)$ = −3.21 (canonical envelope), and $\sigma \sim 2.7$ s, while the second has $T_{\rm eff}$ = 10635 K, $M_\star$ = 0.1869 $M_\odot$, $\log(M_H/M_\star)$ = −2.37 (canonical envelope), and $\sigma \sim 3.0$ s. Both provide comparable average period residuals, with the higher-mass model yielding the slightly smaller σ but lying well below the adopted range of $T_{\rm eff}$, and the lower-mass model lying within that range. Despite the latter being consistent with the adopted $T_{\rm eff}$, the relatively large average period residuals indicate that the fit quality is only moderate. We therefore regard TIC 344130696 as having only a tentative asteroseismological solution: we take the lower-mass model as a representative case but emphasize that its seismological mass should be treated with caution.

3.5. TIC 72637474

As in the case of TIC 156064657, for TIC 72637474 ($T_{\rm eff}$ = 10214 ± 113 K), we performed two separate period-to-period fits based on two different subsets of the detected periods. Set S1 comprises the five periods listed in Table 5 which lie above the 0.1% FAP threshold (∼ 468, 779, 814, 901, 967 s; see Sect. 2.1.5). Set S2 extends S1 by including the additional signal f_5^* at ∼ 1065 s, which becomes acceptable only when the FAP threshold is relaxed to 0.857%.

Using the five periods in S1, we find that the absolute minimum of the quality function over the explored parameter space is reached at $T_{\rm eff}$ = 12930 K, much hotter than the adopted range of $T_{\rm eff}$. Within a narrower interval around the effective temperature of interest, Fig. 6 reveals some possible solutions with comparable quality ($\sigma \sim 3$ *s*). Most of these, however, are clearly hotter or cooler than the adopted range of $T_{\rm eff}$. In contrast, the model with $T_{\rm eff}$ = 10126 K, $M_\star$ = 0.2707 $M_\odot$, $\log(M_H/M_\star)$ = −3.67 (thin envelope), lies within the adopted $T_{\rm eff}$ interval. When repeating the analysis with S2 (i.e., including the additional ∼ 1065 s period), the overall period-fit quality deteriorates across the $T_{\rm eff}$ range of interest. We therefore do not show the S2 results here and adopt the S1 solution with $T_{\rm eff}$ = 10126 K, $M_\star$ = 0.2707 $M_\odot$, and $\log(M_H/M_\star)$ = −3.67 as the representative model for TIC 72637474.

3.6. TIC 188087204

For TIC 188087204 ($T_{\rm eff}$ = 10052 ± 218 K), we performed period-to-period fits using four different subsets of the detected periods (S1–S4; Sect. 2.1.6), each reflecting different assumptions regarding period significance and mode identification. Set S1 comprises the three periods at ∼ 501, 658, and 743 s, corresponding to the frequencies f_0, f_3, and f_5 listed in Table 6, and assumes that f_5 provides the m = 0 component of the putative second triplet, with f_6^* excluded. Set S2 instead adopts f_6^* as the m = 0 component and comprises the periods at ∼ 501, 658, and 747 s (f_0, f_3, and f_6^*). Sets S3 and S4 extend S1 and S2, respectively, by including the additional sub-threshold candidate f_1^* at ∼ 541 s, yielding S3 (∼ 501, 541, 658, and 743 s) and

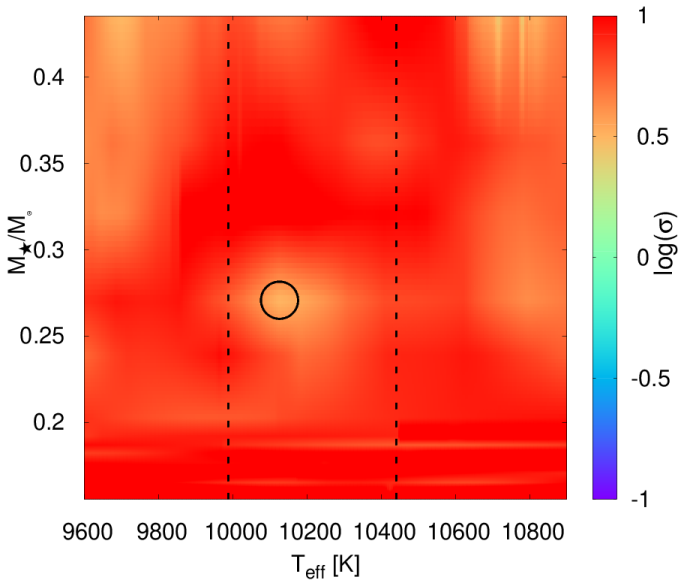

Fig. 6: Same as Fig. 2 but for TIC 72637474, considering the periods from the set S1.

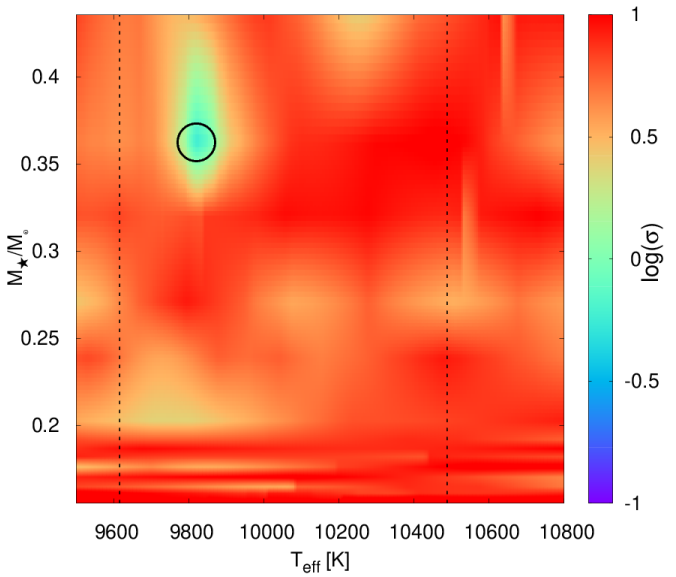

Fig. 7: Same as Fig. 2 but for TIC 188087204, considering the periods from set S1.

S4 (∼ 501, 541, 658, and 747 s). By construction, S1 uses only periods above the nominal FAP threshold, while S2–S4 treat f_1^* and/or f_6^* as plausible, though less secure, modes (Sect. 2.1.6).

Using the three periods in S1 (∼ 501, 658, and 743 s), the best period fit occurs at $T_{\rm eff}$ = 9354 K with a small average period residual, but this temperature lies well below the adopted range, and we therefore discard this solution. Restricting the search to a narrower interval of effective temperature, Fig. 7 reveals a viable solution at $T_{\rm eff}$ = 9820 K, located within the adopted range of $T_{\rm eff}$. It is characterized by $M_\star$ = 0.3624 $M_\odot$, $\log(M_H/M_\star) = -3.62$ (thin envelope), with $\sigma \sim 0.5$ s.

Repeating the procedure with the S2 set (∼ 501, 658, and 747 s), the overall quality of the fits is significantly lower across a relevant range of $T_{\rm eff}$ around that of interest (9500 – 10800 K). The best period fit is found at $T_{\rm eff}$ = 9729 K, $M_\star$ = 0.4352 $M_\odot$ and $\log(M_H/M_\star) = -4.32$ (thin envelope), yielding $\sigma \sim 1$ s. Although this solution is compatible with the adopted $T_{\rm eff}$ interval, the overall $\log\sigma$ map shows a similar structure to that obtained with other subsets but with larger residuals and no additional well-defined minima. For this reason, and to maintain the discussion focused on the most plausible cases, we do not display the S2 map. The S3 set (∼ 501, 541, 658, and 743 s) produces numerous possible solutions scattered throughout the parameter space, all with significantly larger σ than those obtained from S1. The absence of a well-defined minimum and the overall low quality of the fits make this configuration uninformative for our purposes, and we do not display its map either.

The S4 set (∼ 501, 541, 658, and 747 s) yields moderately better results than S2 and S3. As shown in Fig. 8, a possible solution, which is the global minimum of the quality function over the entire explored grid, is found at $T_{\rm eff}$ = 9729 K, $M_\star$ = 0.4352 $M_\odot$, and $\log(M_H/M_\star) = -5.79$ (very-thin envelope), with $\sigma \sim 0.9$ s. This solution lies within the adopted $T_{\rm eff}$ range and the strength of its period match — being the global minimum in our entire grid — makes it a relevant solution. A secondary solution, but with larger residuals ($\sigma \sim 2.1$ s), appears at $T_{\rm eff}$ = 9658 K, $M_\star$ = 0.2390 $M_\odot$, and $\log(M_H/M_\star) = -5.15$ (very-thin envelope).

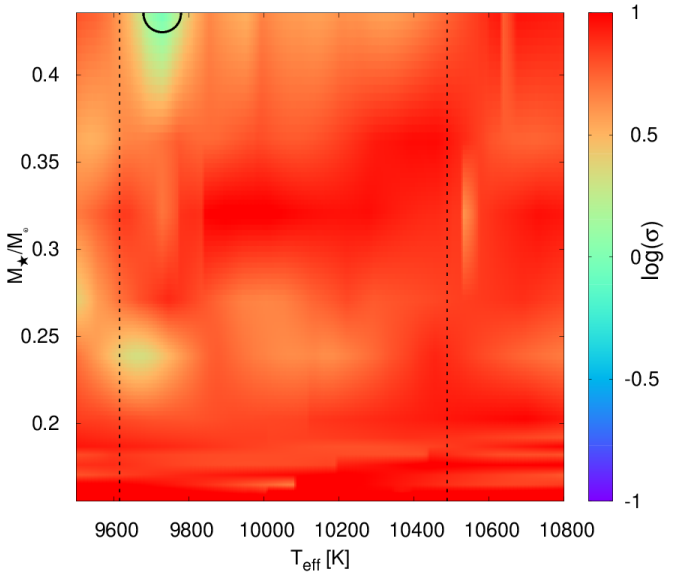

Fig. 8: Same as Fig. 7 but for the periods from set S4.

Overall, we can only conclude that the asteroseismological solutions for TIC 188087204 favor stellar masses between 0.3624 – 0.4352 $M_\odot$, with $T_{\rm eff}$ between 9729 – 9820 K, and H-envelope mass roughly in the range $5 \times 10^{-5} - 2 \times 10^{-4} M_\star$. Among the considered sets, S1 yields the best compromise between period-fit quality and mode identification. Nonetheless, because an acceptable solution also arises from S4, we adopt the above intervals as our conservative asteroseismological inference for this star.

Table 7 summarizes the main results of the asteroseismological analysis of this work, indicating $M_\star^{\rm astero}$, $\log(M_{\rm H}/M_\star)$, and $T_{\rm eff}^{\rm astero}$. Also listed are the adopted atmospheric parameters ($T_{\rm eff}$ and $\log g$), either spectroscopic or photometric, together with the corresponding spectroscopic or photometric masses derived in this work (see next Section).

4. Spectroscopic/photometric masses

We estimated the spectroscopic/photometric stellar masses of our ELMV sample by interpolating their atmospheric parameters ($T_{\rm eff}$, $\log g$) on the evolutionary sequences of Althaus et al. (2013) and Calcaferro et al. (2018b) in the $\log g - \log T_{\rm eff}$ plane (the "Kiel diagram"). For J1112, these parameters are spectroscopic, whereas for the remaining five stars, they are Gaia–based values (Gentile Fusillo et al. 2021). As discussed above, the stellar mass of an LM WD depends on the envelope thickness — thinner envelopes imply higher surface gravities at fixed mass (Calcaferro et al. 2018a; Althaus et al. 2025). To account for this effect, we employed the two-track families cited above, thus spanning from canonical to very thin H envelopes.

As shown in Sect. 3 and summarized in the sixth column of Table 7, our asteroseismological fits indicate that the stars in our sample require H-envelope masses spanning a broad range of thicknesses. One star (J1112) is best reproduced by models with very thin H envelopes, another one (TIC 72637474) is consistent with thin H envelopes, while another (TIC 33717565) allows solutions from canonical to very thin envelopes. TIC 188087204 is best reproduced by models ranging from thin to very thin envelopes, and the remaining two stars (TIC 156064657 and TIC 344130696) are consistent with canonical envelopes. Guided by these results, we computed for each star its spectroscopic/photometric mass by interpolating on the evolutionary tracks matching its H-envelope thickness. For TIC 33717565 and TIC 188087204, for which more than one envelope-thickness regime is possible, we evaluated the consistent cases and report the interval spanned by the two values.

The positions of our target stars in the Kiel diagram are shown in Figure 9, together with the evolutionary sequences employed (solid and dashed lines; Althaus et al. 2013; Calcaferro et al. 2018b, respectively). For clarity, we only display evolutionary tracks corresponding to the canonical and very thin H-envelope limits of our model grid; intermediate envelope masses —although relevant for some of our asteroseismological solutions— are not shown in order to avoid overcrowding the figure. We have also included two evolutionary sequences with 0.130 and 0.140 $M_\odot$ and very thin H envelopes, extracted from Calcaferro et al. (2018a), to cover the domain of low surface gravities of our grid. The resulting spectroscopic/photometric masses, $M_\star^{\rm spec}/M_\star^{\rm phot}$, are listed in the fourth column of Table 7.

Both the spectroscopic and photometric masses inherit uncertainties from the adopted atmospheric parameters. A detailed analysis of the spectroscopic masses will be addressed in a subsequent paper (but see, e.g., Calcaferro et al. 2024a, and references therein). For the five stars with Gaia-based parameters, the photometric masses include an additional layer of model dependence that is specific to this work. Their ($T_{\rm eff}$, $\log g$) values are taken from Gentile Fusillo et al. (2021), who fit Gaia photometry and parallaxes with model atmospheres combined with the canonical LM He-core WD sequences of Serenelli et al. (2001). For our $M_\star^{\rm phot}$ estimates, we instead interpolate these same parameters on the canonical grids of Althaus et al. (2013) and on their thin-envelope extensions (Calcaferro et al. 2018b). As a rough estimate of the associated systematics, we find that the choice of canonical He-core grid changes $M_{\rm phot}$ by only $\sim$ 0.006 $M_\odot$, while adopting very thin instead of canonical H envelopes can shift $M_{\rm phot}$ by up to $\sim$ 0.026 $M_\odot$. This latter effect is relevant only for TIC 33717565 and TIC 188087204, the two stars for which our asteroseismology already yields a range of acceptable solutions rather than a single mass value, and, to a lesser extent, TIC 72637474, since it fits a thin-H envelope model. Nonetheless, a more homogeneous and self-consistent set of photometric masses, computed by fitting multi-band photometry and parallax with our full grid of He-core evolutionary models (including thin-H envelopes when required), will be presented in a forthcoming paper.

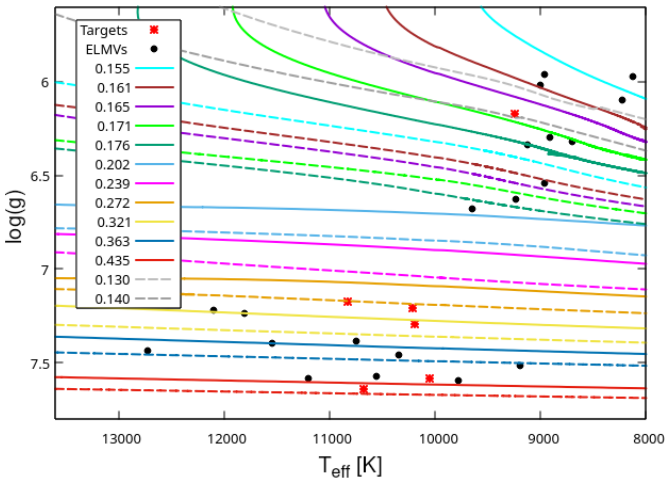

Fig. 9: Kiel diagram for the six ELMVs (red crosses) analyzed in this work. Evolutionary tracks for canonical (solid; Althaus et al. 2013) and very thin (dashed; Calcaferro et al. 2018b) H-envelope masses are included, as well as two artificial evolutionary sequences (with 0.130 and 0.140 $M_\odot$) with very thin H-envelopes. Also displayed are other ELMV targets (black dots).

5. Summary and discussion

In this work, we presented a detailed asteroseismological study of a sample of pulsating LM He-core WDs, based on TESS short- and ultra-short-cadence photometry. One of the targets, J1112, is analyzed with TESS data for the first time, while for most of the remaining objects, we provide new or updated observations. For J1112, we detect two significant periods in the stitched TESS light curves, confirming two of the longest-period modes previously reported by Hermes et al. (2013b). For the other five stars, we found new frequency solutions with respect to previous studies. In particular, for TIC 188087204, we confirm the previously reported triplet around 1521 μHz and uncover evidence for a second, incomplete multiplet with consistent rotational splitting.

We then performed detailed period-to-period fits using our fully evolutionary models and the observed periods for each star (considering alternative period sets for TIC 156064657, TIC 72637474, and TIC 188087204). These fits yield well-constrained asteroseismological solutions for J1112, TIC 156064657, TIC 344130696, and TIC 72637474; for TIC 33717565 and TIC 188087204, we can only delineate ranges of possible solutions. The main properties of the adopted asteroseismological models (stellar mass, H-envelope mass, and effective temperature) are summarized in Table 7.

Our results indicate that the inferred H-envelope masses span a broad range, in line with evolutionary expectations (Calcaferro et al. 2018a; Althaus et al. 2025): one object is best reproduced with a very-thin envelope, one admits a solution with a thin envelope, two admit thin-to-very-thin or canonical-to-very-thin solutions, and two are consistent with canonical envelopes. For J1112, only two independent periods are cur-

Table 7: Main characteristics of the adopted asteroseismological models for the ELMVs analyzed in this work.

Star	$T_{\rm eff}[K]$	$\log(g)$	$M_\star^{\rm spec}/M_\star^{\rm phot}[M_\odot]$	$M_\star^{\rm astero}[M_\odot]$	$\log(M_{\rm H}/M_\star)$	$T_{\rm eff}^{\rm astero}[K]$
J1112*	9240	6.170	0.140	0.1706	−5.30	8922
TIC 156064657	10194	7.295	0.327	0.3624	−3.10	10202
TIC 33717565	10676	7.639	(0.424, 0.445)	(0.1706, 0.3624)	(−5.54, −2.50)	(10660, 11200)
TIC 344130696*	10829	7.177	0.300	0.1869	−2.37	10632
TIC 72637474	10214	7.209	0.292	0.2707	−3.67	10126
TIC 188087204	10052	7.583	(0.415, 0.423)	(0.3624, 0.4352)	(−5.79, −3.62)	(9729, 9820)

Notes. Column 1 lists the star name. Columns 2 and 3 give the adopted atmospheric parameters, effective temperature and surface gravity, either from spectroscopy (J1112) or Gaia-based (the remaining five stars). Column 4 lists the spectroscopic mass for J1112 and the photometric mass for the other stars. Column 5 gives the asteroseismological stellar mass obtained from our period-to-period fits, while columns 6 and 7 list, respectively, the corresponding H-envelope mass and the effective temperature of the adopted asteroseismological model. A range of values is provided when only a range of possible solutions was found. * Tentative asteroseismological solution (see text for details).

rently available; thus, the inferred parameters should be regarded as provisional. Using the atmospheric parameters available for each star (spectroscopic for J1112; Gaia-based for the other five), we derived external mass estimates (also listed in Table 7) by interpolating on evolutionary tracks consistent with the envelope thickness indicated by asteroseismology. For J1112, TIC 156064657, TIC 72637474, and TIC 188087204, the spectroscopic/photometric masses are broadly compatible with the seismological values. In contrast, TIC 33717565 shows a seismological degeneracy in $M_{\rm H}$ (canonical to very thin) and, simultaneously, photometric masses that are high under both envelope assumptions. TIC 344130696 also shows a noticeable discrepancy; here, the seismology is tentative, so we treat its seismological mass as provisional. Finally, we note that unresolved companions may affect Gaia-based photometric parameters and derived photometric masses. Although we find broad agreement between photometric and asteroseismological masses for most targets, spectroscopic follow-up will be valuable to assess this possibility on a star-by-star basis.

A comparison with previous studies is in order. For J1112, Calcaferro et al. (2018b) carried out an asteroseismological study based on the five longest periods reported by Hermes et al. (2013b) from ground-based observations (two of which we confirm in this work with space-based data). Using the same fully evolutionary models employed in the present work, they obtained a representative asteroseismological model characterized by $M_\star = 0.1612\ M_\odot$, in contrast with our current result, $M_\star = 0.1706\ M_\odot$. This modest discrepancy can be attributed to differences in the adopted set of fitted periods. Regarding the other five analyzed stars, the only other available asteroseismological study is that of Romero et al. (2022). Their analysis was performed under the assumption that all targets are ZZ Ceti stars (i.e., pulsating DA WDs with CO cores), and thus employed CO–core evolutionary models. This naturally leads to higher inferred stellar masses. For TIC 156064657, TIC 344130696, and TIC 72637474, our best-fitting models have $M_\star = 0.3624$, 0.1869, and 0.2707 $M_\odot$, respectively, whereas Romero et al. (2022) reported 0.493, 0.632, and 0.542 $M_\odot$. For TIC 33717565 and TIC 188087204, where our analysis yields mass ranges of 0.1706 – 0.3624 and 0.3624 – 0.4352 $M_\odot$, Romero et al. (2022) found 0.609 and 0.493 $M_\odot$, respectively. The discrepancies, particularly for the least massive cases, are therefore not unexpected and reflect the different assumptions about core composition and evolutionary history. It is worth stressing that our revised frequency solutions (Sect. 2.1), which imply a different set of fitted periods, may also lead to a different preferred asteroseismological model within a given evolutionary grid.

The analysis presented here represents a first step towards a systematic asteroseismological characterization of pulsating LM WDs with TESS data. In this work, we have focused on a subset of ELMVs for which TESS already reveals relatively clean frequency spectra and for which basic atmospheric parameters are available, making them particularly suitable to explore the capabilities and limitations of our modelling approach. Extending the same methodology to the remaining ELMV candidates observed by TESS, many of which will involve more complex or lower-S/N pulsation spectra, will require a dedicated analysis of their light curves and frequency content and is beyond the scope of this first study. Future space-based photometric missions are also expected to expand the sample of candidates and, in many cases, provide richer mode sets that enable more robust mode identification and stronger constraints on theoretical models (e.g., Uzundag et al. 2025).

Acknowledgements. M. U. gratefully acknowledges funding from the Research Foundation Flanders (FWO) by means of a junior postdoctoral fellowship (grant agreement No. 1247624N). This paper includes data collected with the TESS mission, obtained from the MAST data archive at the Space Telescope Science Institute (STScI). Funding for the TESS mission is provided by the NASA Explorer Program. This research has made use of NASA's Astrophysics Data System Bibliographic Services, and the SIMBAD and VizieR databases, operated at CDS, Strasbourg, France.

References

Althaus, L. G., Calcaferro, L. M., Córsico, A. H., & Brown, W. R. 2025, A&A, 699, A280
Althaus, L. G., Camisassa, M. E., Miller Bertolami, M. M., Córsico, A. H., & García-Berro, E. 2015, A&A, 576, A9
Althaus, L. G., Córsico, A. H., Isern, J., & García-Berro, E. 2010, A&A Rev., 18, 471
Althaus, L. G., Gil-Pons, P., Córsico, A. H., et al. 2021, A&A, 646, A30
Althaus, L. G., Miller Bertolami, M. M., & Córsico, A. H. 2013, A&A, 557, A19
Althaus, L. G., Panei, J. A., Romero, A. D., et al. 2009, A&A, 502, 207
Althaus, L. G., Serenelli, A. M., Panei, J. A., et al. 2005, A&A, 435, 631
Amaro-Seoane, P., Audley, H., Babak, S., et al. 2017, arXiv e-prints, arXiv:1702.00786
Antunes Amaral, L., Munday, J., Vučković, M., et al. 2024, A&A, 685, A9
Baran, A. S. & Koen, C. 2021, Acta Astron., 71, 113
Bedin, L. R., Salaris, M., Anderson, J., et al. 2015, MNRAS, 448, 1779
Bell, K. 2022, Pyriod: Period detection and fitting routines, Astrophysics Source Code Library, record ascl:2207.007
Bell, K. J. 2026, in Encyclopedia of Astrophysics, Volume 3, Vol. 3, 75–90
Bell, K. J., Gianninas, A., Hermes, J. J., et al. 2017, ApJ, 835, 180
Bell, K. J., Pelisoli, I., Kepler, S. O., et al. 2018, A&A, 617, A6
Bildsten, L., Shen, K. J., Weinberg, N. N., & Nelemans, G. 2007, ApJ, 662, L95
Bischoff-Kim, A. 2023, ApJ, 958, 101

Bischoff-Kim, A., Provencal, J. L., Bradley, P. A., et al. 2019, ApJ, 871, 13
Bognár, Z. & Sódor, Á. 2024, A&A, 684, A76
Brickhill, A. J. 1991, MNRAS, 251, 673
Brown, W. R., Gianninas, A., Kilic, M., Kenyon, S. J., & Allende Prieto, C. 2016, ApJ, 818, 155
Brown, W. R., Kilic, M., Allende Prieto, C., Gianninas, A., & Kenyon, S. J. 2013, ApJ, 769, 66
Brown, W. R., Kilic, M., Allende Prieto, C., & Kenyon, S. J. 2010, ApJ, 723, 1072
Brown, W. R., Kilic, M., Allende Prieto, C., & Kenyon, S. J. 2012, ApJ, 744, 142
Brown, W. R., Kilic, M., Kosakowski, A., et al. 2020, ApJ, 889, 49
Brown, W. R., Kilic, M., Kosakowski, A., & Gianninas, A. 2022, ApJ, 933, 94
Calcaferro, L. M., Althaus, L. G., & Córsico, A. H. 2018a, A&A, 614, A49
Calcaferro, L. M., Córsico, A. H., & Althaus, L. G. 2017, A&A, 607, A33
Calcaferro, L. M., Córsico, A. H., Althaus, L. G., & Bell, K. J. 2021, A&A, 647, A140
Calcaferro, L. M., Córsico, A. H., Althaus, L. G., Romero, A. D., & Kepler, S. O. 2018b, A&A, 620, A196
Calcaferro, L. M., Córsico, A. H., Uzundag, M., et al. 2024a, A&A, 691, A194
Calcaferro, L. M., Sowicka, P., Uzundag, M., et al. 2024b, A&A, 686, A140
Camisassa, M. E., Althaus, L. G., Torres, S., et al. 2021, A&A, 649, L7
Camisassa, M. E., Raddi, R., Althaus, L. G., et al. 2022, MNRAS, 516, L1
Córsico, A. H. & Althaus, L. G. 2006, A&A, 454, 863
Córsico, A. H. & Althaus, L. G. 2014a, A&A, 569, A106
Córsico, A. H. & Althaus, L. G. 2014b, ApJ, 793, L17
Córsico, A. H. & Althaus, L. G. 2016, A&A, 585, A1
Córsico, A. H., Althaus, L. G., Kepler, S. O., Costa, J. E. S., & Miller Bertolami, M. M. 2008, A&A, 478, 869
Córsico, A. H., Althaus, L. G., Miller Bertolami, M. M., & Bischoff-Kim, A. 2012, A&A, 541, A42
Córsico, A. H., Althaus, L. G., Miller Bertolami, M. M., & Kepler, S. O. 2019, A&A Rev., 27, 7
Córsico, A. H., Althaus, L. G., Miller Bertolami, M. M., & Werner, K. 2007a, A&A, 461, 1095
Córsico, A. H., Miller Bertolami, M. M., Althaus, L. G., Vauclair, G., & Werner, K. 2007b, A&A, 475, 619
Cummings, J. D., Kalirai, J. S., Choi, J., et al. 2019, ApJ, 871, L18
Doherty, C. L., Gil-Pons, P., Lau, H. H. B., et al. 2014, MNRAS, 441, 582
El-Badry, K., Rix, H.-W., & Weisz, D. R. 2018, ApJ, 860, L17
Fontaine, G. & Brassard, P. 2008, PASP, 120, 1043
García-Berro, E. & Oswalt, T. D. 2016, New A Rev., 72, 1
Gentile Fusillo, N. P., Tremblay, P. E., Cukanovaite, E., et al. 2021, MNRAS, 508, 3877
Giammichele, N., Charpinet, S., Fontaine, G., et al. 2018, Nature, 554, 73
Gianninas, A., Curd, B., Fontaine, G., Brown, W. R., & Kilic, M. 2016, ApJ, 822, L27
Gianninas, A., Kilic, M., Brown, W. R., Canton, P., & Kenyon, S. J. 2015, ApJ, 812, 167
Guidry, J. A., Vanderbosch, Z. P., Hermes, J. J., et al. 2021, ApJ, 912, 125
Han, Z., Tout, C. A., & Eggleton, P. P. 2000, MNRAS, 319, 215
Hermes, J. J., Montgomery, M. H., Gianninas, A., et al. 2013a, MNRAS, 436, 3573
Hermes, J. J., Montgomery, M. H., Winget, D. E., et al. 2013b, ApJ, 765, 102
Hermes, J. J., Montgomery, M. H., Winget, D. E., et al. 2012, ApJ, 750, L28
Iben, I., J. & Tutukov, A. V. 1984, ApJS, 54, 335
Irrgang, A., Geier, S., Heber, U., et al. 2021, A&A, 650, A102
Istrate, A. G., Marchant, P., Tauris, T. M., et al. 2016, A&A, 595, A35
Jewett, G., Kilic, M., Moss, A., et al. 2025, ApJ, 994, 255
Kepler, S. O., Pelisoli, I., Koester, D., et al. 2016, MNRAS, 455, 3413
Kilic, M., Brown, W. R., Allende Prieto, C., et al. 2011, ApJ, 727, 3
Kilic, M., Brown, W. R., Allende Prieto, C., et al. 2012, ApJ, 751, 141
Kilic, M., Hermes, J. J., Córsico, A. H., et al. 2018, MNRAS, 479, 1267
Kilic, M., Hermes, J. J., Gianninas, A., & Brown, W. R. 2015, MNRAS, 446, L26
Kilic, M., Munn, J. A., Harris, H. C., et al. 2017, ApJ, 837, 162
Kosakowski, A., Brown, W. R., Kilic, M., et al. 2023, ApJ, 950, 141
Kosakowski, A., Kilic, M., Brown, W. R., & Gianninas, A. 2020, ApJ, 894, 53
Lee, J. W., Hong, K., Kim, H.-Y., & Park, J.-H. 2022, MNRAS, 515, 4702
Li, Z., Chen, X., Chen, H.-L., & Han, Z. 2019, ApJ, 871, 148
Lopez, I. D., Hermes, J. J., Calcaferro, L. M., et al. 2021, ApJ, 922, 220
Maxted, P. F. L., Serenelli, A. M., Marsh, T. R., et al. 2014, MNRAS, 444, 208
Maxted, P. F. L., Serenelli, A. M., Miglio, A., et al. 2013, Nature, 498, 463
Parsons, S. G., Brown, A. J., Littlefair, S. P., et al. 2020, Nature Astronomy, 4, 690
Pelisoli, I., Kepler, S. O., Koester, D., et al. 2018, MNRAS, 478, 867
Prada Moroni, P. G. & Straniero, O. 2009, A&A, 507, 1575
Ricker, G. R., Winn, J. N., Vanderspek, R., et al. 2015, Journal of Astronomical Telescopes, Instruments, and Systems, 1, 014003
Romero, A. D., Córsico, A. H., Althaus, L. G., et al. 2012, MNRAS, 420, 1462
Romero, A. D., Kepler, S. O., Hermes, J. J., et al. 2022, MNRAS, 511, 1574
Romero, A. D., Kepler, S. O., Oliveira da Rosa, G., & Hermes, J. J. 2025, ApJ, 984, 112
Saumon, D., Blouin, S., & Tremblay, P.-E. 2022, Phys. Rep., 988, 1
Schwab, J. 2021, ApJ, 906, 53
Serenelli, A. M., Althaus, L. G., Rohrmann, R. D., & Benvenuto, O. G. 2001, MNRAS, 325, 607
Serenelli, A. M., Althaus, L. G., Rohrmann, R. D., & Benvenuto, O. G. 2002, MNRAS, 337, 1091
Steinfadt, J. D. R., Bildsten, L., & Arras, P. 2010, ApJ, 718, 441
Strickler, R. R., Cool, A. M., Anderson, J., et al. 2009, ApJ, 699, 40
Su, J. & Li, Y. 2023, ApJ, 943, 113
Sun, M. & Arras, P. 2018, ApJ, 858, 14
Tremblay, P. E., Cummings, J., Kalirai, J. S., et al. 2016, MNRAS, 461, 2100
Tremblay, P.-E., Gianninas, A., Kilic, M., et al. 2015, ApJ, 809, 148
Unno, W., Osaki, Y., Ando, H., Saio, H., & Shibahashi, H. 1989, Nonradial oscillations of stars, ed. T. University of Tokyo Press
Uzundag, M., Corsico, A. H., Jannsen, N., et al. 2025, arXiv e-prints, arXiv:2511.19196
Uzundag, M., Córsico, A. H., Kepler, S. O., et al. 2022, MNRAS, 513, 2285
Uzundag, M., De Gerónimo, F. C., Córsico, A. H., et al. 2023, MNRAS, 526, 2846
Van Grootel, V., Fontaine, G., Brassard, P., & Dupret, M.-A. 2013, ApJ, 762, 57
Wang, K., Németh, P., Luo, Y., et al. 2022, ApJ, 936, 5
Wang, K., Zhang, X., & Dai, M. 2020, ApJ, 888, 49
Webbink, R. F. 1984, ApJ, 277, 355
Winget, D. E. & Kepler, S. O. 2008, ARA&A, 46, 157

Appendix A: Lists of selected objects

Here we provide basic information about the objects analyzed in this paper.

Table A.1: Sample of ELMVs analyzed in this work. Column (a) is the star's name, column (b) indicates its Gaia DR3 ID, column (c) and (d) show the equatorial coordinates. Column (e) display the DR3 *Gaia* apparent magnitude. Column (f) and (g) indicate the effective temperature and gravity (spectroscopic for J1112, Gaia-based for the rest), while column (h) is the reference.

Star	GAIA ID	RA (deg)	DEC (deg)	G (mag)	$T_{\rm eff}$ [K]	$\log(g)$ [cgs]	Reference
(a)	(b)	(c)	(d)	(e)	(f)	(g)	(h)
J1112	3963587822967516032	11 : 12 : 15.80	+11 : 17 : 45.1	16, 34	9240 ± 140	6.17 ± 0.060	Hermes et al. (2013b)
TIC 156064657	4974784825671467648	00 : 37 : 23.75	−48 : 21 : 55.9	16, 57	10194 ± 132	7.295 ± 0.034	Romero et al. (2022)
TIC 33717565	4627855367706529152	04 : 05 : 36.39	−76 : 28 : 28.1	16.50	10676 ± 173	7.639 ± 0.031	Romero et al. (2022)
TIC 344130696	6365271657299575680	18 : 37 : 08.30	−76 : 59 : 05.9	15.39	10829 ± 116	7.177 ± 0.018	Romero et al. (2022)
TIC 72637474	5020319141229055360	02 : 08 : 07.86	−29 : 31 : 38.8	15, 90	10214 ± 113	7.209 ± 0.025	Romero et al. (2022)
TIC 188087204	5470271185153118208	10 : 46 : 27.80	−25 : 12 : 15.8	16.83	10052 ± 218	7.583 ± 0.055	Romero et al. (2022)

Appendix B: Methodology for re-computing FAP for sub-threshold peaks

When a candidate peak falls below the nominal 0.1% detection threshold, we reassess its significance by computing a new false-alarm probability (FAP) using the analytic model of Baran & Koen (2021). Their Eq. (5) gives the percentile u_p of the *median-standardized* amplitude-spectrum maximum U as a function of the number of data points N and FAP p. In practice, we measure u_p for a candidate by normalizing the peak amplitude to the spectrum's local/median noise level (consistent with our periodogram workflow), and then infer p by inverting Eq. (5). This inversion is closed-form (a Gumbel-distribution), so evaluation is straightforward once u_p and N are specified.

Inputs. (1) **Cadence-informed N.** Following Baran & Koen (2021), we adopt the per-sector data-point counts $N = 116{,}640$ for 20 s (ultra-short) cadence and $N = 19{,}440$ for 120 s (short) cadence.
(2) **Search bandwidth.** If the test is confined to a subrange of the spectrum (e.g., a white-dwarf g-mode band), we replace N by an effective $N_{\rm eff} = f\,N$, where f is the tested frequency range as a fraction of $(0, \nu_{\rm Nyq}]$. This aligns the calculation with the actual number of independent frequencies being interrogated.
(3) **Measured u_p.** For each candidate, we compute the percentile-like height u_p from the median standardized amplitude spectrum of the (residual) time series used to test that peak.

Computation. With u_p and N (or $N_{\rm eff}$) in hand, we invert Eq. (5) of Baran & Koen (2021) to obtain

$$p \;=\; 1 - \exp\!\Big(-\exp\!\big(\tfrac{1.05\,\ln N - (u_p/1.201)^2}{1.04}\big)\Big).$$

We report this p as the recalculated FAP for that candidate.